

Automatic Detection of Marine Gas Seeps Using an Interferometric Sidescan Sonar

Ann Elisabeth Albright Blomberg, Torstein Olsmo Sæbø, *Senior Member, IEEE*,
Roy Edgar Hansen, *Senior Member, IEEE*, Rolf Birger Pedersen, and Andreas Austeng, *Member, IEEE*

Abstract—There is a significant need for reliable, cost-effective, and preferably automatic methods for detecting and monitoring marine gas seeps. Seeps at the seafloor may originate from natural sources including sediments releasing biogenic methane and volcanoes releasing CO₂, or from man-made constructions such as pipelines or well heads, and potentially also from subseafloor CO₂ storage sites. Improved seep detection makes it possible to estimate the amount of greenhouse gases entering the oceans, and to promptly detect and address potential leaks to reduce environmental and economical consequences. Sonar is an excellent tool for seep detection due to the strong acoustic backscatter properties of gas-filled bubbles in water. Existing methods for acoustic seep detection include multibeam and sidescan surveying, as well as active and passive sensors mounted on a stationary platform. In this work, we develop a new method for automatic seep detection using an interferometric sidescan sonar. We apply signal processing techniques combined with knowledge about acoustical and spatial properties of seeps for improved detectability. The proposed method fills an important gap in existing technology—the ability to automatically detect a seep during a single pass with an autonomous underwater vehicle (AUV) equipped with an interferometric sidescan sonar. Results from simulations as well as field data from two leaking abandoned wells in the North Sea indicate that small seeps are consistently detected on a sandy seafloor even when the observation time is limited (a single pass with the AUV). We explore the detection capability for different seafloor types ranging from silt to gravel.

Index Terms—Automatic leakage detection, carbon capture and storage (CCS) monitoring, coherence, gas seep detection, interferometric sonar, sidescan sonar.

I. INTRODUCTION

IN recent decades, there has been an increasing interest in monitoring the seafloor to detect, monitor, and quantify marine gas seeps. Potential leakage scenarios that require monitoring include natural seepage of methane and CO₂ into the oceans, leakage from man-made constructions related to oil and gas production, and potential leakage events related to carbon capture and storage (CCS). Detecting gas seeps at the seafloor at

Manuscript received March 1, 2016; revised June 21, 2016; accepted July 12, 2016. This work was supported by the Norwegian Research Council under Grants to the Digital Signal Processing and Image analysis (DSB) group at the University of Oslo, Centre for Geobiology and FME SUCCESS, and by the ECO2 project.

Associate Editor: D. Simons

A. E. A. Blomberg, A. Austeng, and R. E. Hansen are with the Digital Signal Processing and Image Analysis Group, Department of Informatics, University of Oslo, Oslo 0316, Norway (e-mail: aebloambe@ifi.uio.no; andrea@ifi.uio.no; Roy-Edgar.Hansen@ffi.no).

R. E. Hansen and T. O. Sæbø are with the Norwegian Defence Research Establishment (FFI), Kjeller N-2027, Norway (e-mail: Torstein-Olsmo.Sabo@ffi.no).

R. B. Pedersen is with the Centre for Geobiology, Department of Earth Science, University of Bergen, Bergen N-5020, Norway (e-mail: rolf.pedersen@geo.uib.no).

Digital Object Identifier 10.1109/JOE.2016.2592559

an early stage is of importance to prevent environmental as well as economical consequences, and to gain a better understanding of the amount of greenhouse gases seeping into the oceans and potentially reaching the atmosphere [1], [2].

The long range capabilities of sonars combined with the large contrast in acoustic impedance between free gas and water makes sonar a useful tool for cost-effective monitoring of the seafloor [3], [4]. Existing or proposed methods for acoustic gas seep detection include single-beam and multibeam sonar [3], [5]–[7] split-beam sonar [11], sidescan sonar [8], and passive sonar [9], [10]. Several studies demonstrate the potential of using broadband or multifrequency sonar data for seep characterization, taking advantage of the frequency-dependent properties of gas bubbles [11], [12].

While gas seeps are generally observable in sonar imagery, current methods rely heavily on either an operator's ability to scrutinize the data and to recognize gas seeps because of their characteristic appearance, or in the case of stationary systems, a long observation time to achieve reliable automatic detection. Limited efforts have so far been directed toward optimizing active sonar methods for reliable and potentially automatic seep detection.

In this paper, which is an extension of the preliminary study in [13], we investigate the potential benefits of using an interferometric sidescan sonar mounted on an autonomous underwater vehicle (AUV) for automatic gas seep detection. Combining array signal processing techniques with an understanding of the acoustical and spatial properties of rising bubbles, a seep is recognized instantly (in a single ping) as a region of high image intensity and low interferometric coherence. The proposed method can be applied to any interferometric sidescan sonar system, including synthetic aperture sonar (SAS) systems operated in sidescan mode. We use the AUV-mounted HISAS 1030 sonar [14], which is an interferometric SAS developed for high-resolution imagery and bathymetry of the seafloor.

We motivate our work in Section II-A, and offer a brief overview of existing acoustic technology aimed at gas seep detection and monitoring in Section II-B. Section II-C includes a brief overview of the acoustical and spatial properties of gas seeps which are relevant for the proposed seep detection method. In Section II-D, we describe how key features of a seep (high target strength as well as low interferometric coherence) can be measured using an interferometric sidescan sonar. In Section III, we propose an algorithm to automatically detect image pixels originating from a seep location. We have carried out a set of simulations described in Section IV, which we use to analyze the interferometric sidescan response from different gas seeps and with varying seafloor characteristics. We present

results from the simulations in Section V, and in Section VI, we present results from field data acquired at two abandoned North Sea wells. Finally, we discuss our findings in Section VII, and summarize our conclusions in Section VIII.

II. BACKGROUND

A. Leakage Scenarios and the Need for Monitoring

Natural seepage of methane and CO₂ is common in many regions where geological structures such as pockmarks, mud volcanoes, faults, or salt domes allow these greenhouse gases to penetrate the seafloor and enter the water column and potentially also the atmosphere [15]. Rising seawater temperatures may trigger the release of large amounts of gas currently trapped in permafrost [16]–[18]. There is also an increased awareness within the oil and gas industry as well as in the CCS community regarding the need for accurate and reliable monitoring methods. According to the European Union (EU) directive on CO₂ storage [19], the Member States are required to monitor the injection facilities, the storage complex, and where relevant the surrounding environment according to specific guidelines. The main CCS monitoring strategy today is seismic surveying carried out once every one to three years. Time-lapse seismic studies reveal large-scale trends and the location and spreading of the CO₂ plume within the reservoir [20]. Several recent research projects, including the SUCCESS center [21], the EU research project ECO2 [22], and the QICS (quantifying and monitoring potential ecosystem impacts of geological carbon storage) project [23], highlight the need for more systematic and detailed monitoring of the seafloor and water column to complement seismic surveys. In [24], Blackford *et al.* summarize the conclusions from the controlled CO₂ release project (QICS) and discuss CCS monitoring strategies, highlighting the need for a multidisciplinary and site-specific monitoring approach.

B. Acoustic Methods for Seep Detection

The ability to detect marine gas seeps using sonars was discovered several decades ago. One of the earliest studies is from 1974 by Sweet [25], and demonstrates that a high-resolution sub-bottom acoustic profiler can be used to detect bubble seeps in the ocean. Since then, a range of studies have documented the ability to detect seeps acoustically. In recent years, multi-beam sonars have emerged as the most common method of surveying, significantly improving the coverage rate compared to single-beam surveys [3], [5], [26]. Traditionally, most sonar systems used in seep observation and detection are mounted on the hull of a ship. AUV-mounted sonars have also been proposed as they offer improved image quality (resolution) compared to their ship-mounted counterpart [6].

Several recent works demonstrate the use of sonar to derive specific properties of oil and gas seeps in addition to merely detecting their presence. In [11], Weber *et al.* show how the EK60 split-beam echosounder can be used to estimate the seep trajectory as it rises through the water column. They also offer a means to constrain the bubble size estimates when multiple

frequencies are used. In [12], Weber *et al.* use a calibrated single-beam echosounder to estimate the concentration as well as the flow rate of an oil seep, and in [27], Leifer and Tang make an interesting comparison between optical and passive acoustical measurements. Stationary acoustic systems have been proposed for detailed monitoring of a single seep or a collection of closely spaced seeps [28], [29], and lander-based systems combining a range of sensors including sonars are emerging as a research tool for environmental engineering. These methods rely on long observation periods to collect enough data to estimate background noise levels and detect seep events. Seep-related gas bubbles also generate characteristic acoustic emissions which can be measured passively and used to detect, localize, and quantify a seep [9], [10], [30].

The method proposed in this paper is based on the use of an interferometric sidescan sonar, and can be implemented on a stationary or a moving platform. Examples and discussions in this paper focus on the latter, where the sonar system is mounted on an AUV.

C. Acoustic Backscatter Properties of Gas Bubbles

Acoustic methods are well suited for detecting bubbles in water, due to the high contrast in acoustic impedance between water and gas. The acoustic response of gas-filled bubbles is highly frequency dependent, with a strong peak at the resonance frequency [4], [31], [32]. The backscattered cross section is defined as the total scattered power divided by the incident planewave intensity. For a single gas bubble with radius a and $ka < 1$, it can be approximated as [4]

$$\sigma_{\text{BS}} = \frac{a^2}{\left[\left(\frac{f_0}{f} \right)^2 - 1 \right]^2 + \delta^2} \quad (1)$$

where f is the transmit frequency, f_0 is the resonant frequency, k is the acoustic wave number, and δ is a damping term. The resonant frequency for an air-filled bubble at water depth z can be estimated as

$$f_0 = \frac{1}{2\pi a} \sqrt{\frac{3\gamma P_w}{\rho_w}} \quad (2)$$

where γ is the adiabatic constant for air (≈ 1.4), ρ_w is the water density, and P_w is the hydrostatic pressure measured in Pascal. The values for ρ_w , P_w , and f_0 can be approximated as 10^3 kg m^{-3} , $10^5(1 + z/10)$, and $3.25/a\sqrt{1 + 0.1z}$, respectively. The damping term δ is a sum of three damping terms: the reradiation term, the thermal damping term, and the viscous damping term. Its expression is complex, but for frequencies between 1 and 100 kHz, it can be approximated as $0.03(f_k/f_1)^{0.3}$, where $f_1 = 1 \text{ Hz}$, and f_k is the frequency in kilohertz [4, Ch. 3.3.3]. We use this approximation, although the HISAS operates at the upper bounds of its validity.

The target strength (TS), measured in decibels, is defined as the effective backscattering cross section (i.e., the backscattering cross section in the direction of the sonar receiver θ_i). For a bubble with omnidirectional scattering, the target strength can

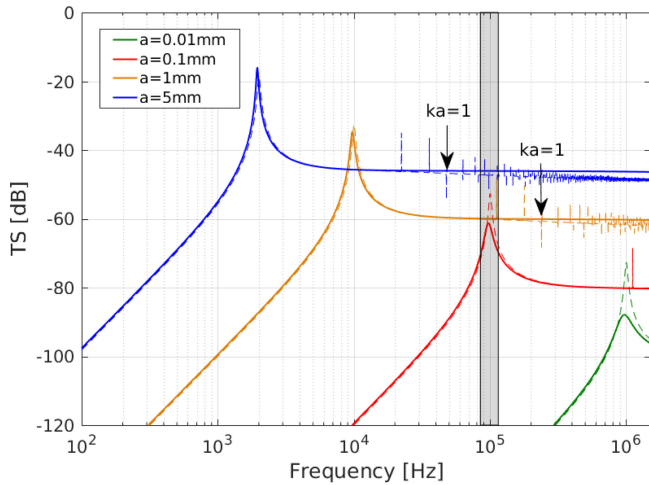


Fig. 1. TS for single, spherical air bubbles with radii ranging from $a = 0.01$ mm to $a = 5$ mm, at a water depth of 80 m. The solid lines represent the TS approximation in (3), valid for $ka < 1$. The dashed lines are included to indicate the modal series solution valid also for large ka . The shaded gray area indicates the operating frequency range of the HISAS sonar.

be computed as

$$TS = 10 \log \left(\frac{\sigma_{BS}}{A_1} \right) \quad (3)$$

where A_1 is the unit section (1 m^2).

Fig. 1 shows the predicted TS, computed using (3), from a single air-filled bubble in water at a depth of 80 m, with bubble radii ranging from $a = 0.01$ mm to $a = 5$ mm. The solid lines indicate the TS computed using (3) and (1), valid for $ka < 1$. For the larger bubbles ($a = 1$ mm and $a = 5$ mm) insonified at high frequencies, ka is larger than 1 and (1) is no longer a valid approximation to the exact modal solution to the scattering from a fluid sphere described by Anderson [33]. The mathematically converged modal series solution also valid for large ka (including 35 modal terms, and with density and sound-speed contrast $g = 0.0118$ and $h = 0.2274$) is indicated by the dashed lines in Fig. 1. While the modal series solution is exact, it does not include the important damping term δ , resulting in unrealistically high and sharp resonant peaks. The smaller dips and peaks for large ka in the modal series solution are related to modal interferences, and are only expected to coincide with the measured response in the ideal case of clean, perfectly spherical bubbles. The deviation between the TS curve computed using (1) and (3), and the modal series solution is about 1 dB in the frequency range of the HISAS, and has no implications for the detection method proposed here. For quantification purposes using a calibrated sonar system, care should be taken to use the correct TS model for all relevant ka .

The shaded area in Fig. 1 ranges from 85 to 115 kHz and corresponds to the frequency range of the HISAS sonar. At this depth and frequency range, the bubble resonance size lies in the interval $0.08 \text{ mm} > a > 1.08 \text{ mm}$. Although the bubble size distribution for different leakage scenarios is not well documented, several studies have observed bubble sizes of about 1–8 mm [34]–[36]. Only the smaller of these bubbles are resonant at the

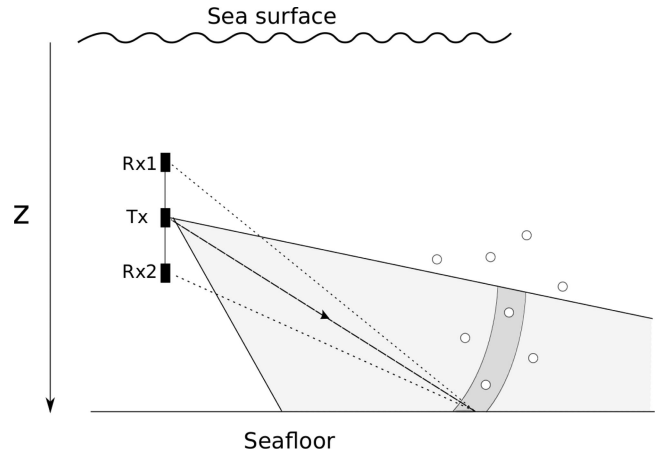


Fig. 2. In an interferometric system with a transmitter (Tx) and two receivers (Rx1 and Rx2), the interferometric coherence drops when there are multiple scatterers with comparable backscatter strength at different heights above the sea floor within the correlation window (dark gray region). In this case, two bubbles are present in addition to the sea floor.

frequency span of the HISAS sonar. In a seep with bubbles of different sizes, the larger bubbles may still contribute significantly to the total reflections. As illustrated by Fig. 1, bubbles with 1- and 5-mm radii both have a higher TS within the HISAS frequency band (shaded area) than a bubble with radius 0.1 mm, even though the latter is resonant while the two former are not.

Fig. 1 is valid for a single, spherical bubble. Rising gas bubbles are rarely perfectly spherical. For nonspherical bubbles, a small shift in the resonant peak as well as changes in the TS is predicted [37]–[40].

D. Interferometric Sidescan Sonar for Seep Detection

An interferometric sidescan sonar produces seafloor imagery as well as an estimate of the seafloor topography. Fig. 2 illustrates a typical configuration, with a transmitter (Tx) and two receivers (Rx1 and Rx2) separated by a vertical baseline. The transmitter sends an acoustic pulse toward the seafloor, and the scattered reflections are recorded by the two receivers. One image is formed for each receiver by beamforming the recorded time series, x_1 and x_2 for each ping, and arranging these side by side. The seafloor height relative to the sonar can be estimated from the pair of images by computing the difference in arrival times at the two receivers [41]. In this work, we demonstrate how an interferometric sidescan sonar can also be used as an effective tool for marine gas seep detection.

1) Sidescan Sonar Image Intensity From a Gas Seep

The sidescan sonar image intensity is typically high in the presence of a gas seep, due to the strong backscatter properties of gas bubbles in water. The visibility of a gas seep in a sonar image depends on a number of factors including the bubble flux, bubble size distribution, seafloor characteristics, and sonar frequency. The imaging geometry (range and viewing angle) and the size of the resulting sonar footprint also have a significant impact. Although the backscatter strength from a collection of bubbles is high, a seep may occupy only a small portion of the

sonar footprint, such that the reflections from a single ping will be a combination of reflections from the seafloor and from the seep.

While high image intensity may indicate the presence of a seep, this alone is not enough information on which to base an automatic seep detection method. Strong reflectors such as stones, shells, or other objects on the seafloor may easily be misinterpreted as potential gas seeps.

2) Interferometric Coherence From a Gas Seep

The interferometric coherence, or spatial coherence between the images formed by the two receiver arrays, represents an additional feature which makes robust automatic seep detection possible. The interferometric coherence γ can be computed for each ping, and is defined as the peak normalized cross correlation between the two complex time series x_1 and x_2 [42]

$$\gamma_{x_1, x_2} = \max_{\tau} \left\{ \frac{|E \{x_1(t)x_2^*(t - \tau)\}|}{\sqrt{E \{|x_1(t)|^2\} E \{|x_2(t)|^2\}}} \right\} \quad (4)$$

where $*$ denotes the complex conjugation operation, and $E \{ \dots \}$ is the statistical expectation. The received time series x_1 and x_2 consist of a signal component s and a noise component n . A basic assumption is that s_1 and s_2 represent echoes from the same region on the seafloor such that s_2 is a delayed replica of s_1

$$\begin{aligned} x_1(t) &= s_1(t) + n_1(t) \\ x_2(t) &= s_2(t) + n_2(t) \\ &= s_1(t - \tau) + n_2(t). \end{aligned} \quad (5)$$

In practice, the statistical expectations in (4) are not known, and the interferometric coherence for each image pixel is estimated by averaging over N neighboring image pixels

$$\gamma_{x_1, x_2} = \max_k \frac{|\sum_{n=1}^N x_1[n]x_2^*[n - k]|}{\sqrt{\sum_{n=1}^N |x_1[n]|^2 |x_2[n]|^2}} \quad (6)$$

where k represents a sample time delay [41].

The interferometric coherence can be directly related to the signal-to-noise ratio (SNR) [43]. High interferometric coherence is a prerequisite for successful SAS imaging, and may be used to estimate the useful SAS imaging range [44]. The coherence is low in the following cases:

- 1) the noise component n dominates the signal component s ;
- 2) the signal component s_2 is not a delayed replica of s_1 .

Case 1) occurs at far range where the signal intensity drops, in shadow regions, and where there is a lack of signal energy, and in the presence of multipath propagation or strong external noise sources. Case 2) occurs when the vertical receiver separation is too large (baseline decorrelation), and when there are several scatterers of comparable strength at different heights within the correlation window (layover). Layover is common in areas with extreme topography, but also occurs when reflections from the seafloor are combined with reflections from bubbles with significant backscatter strength relative to the seafloor. Fig. 2

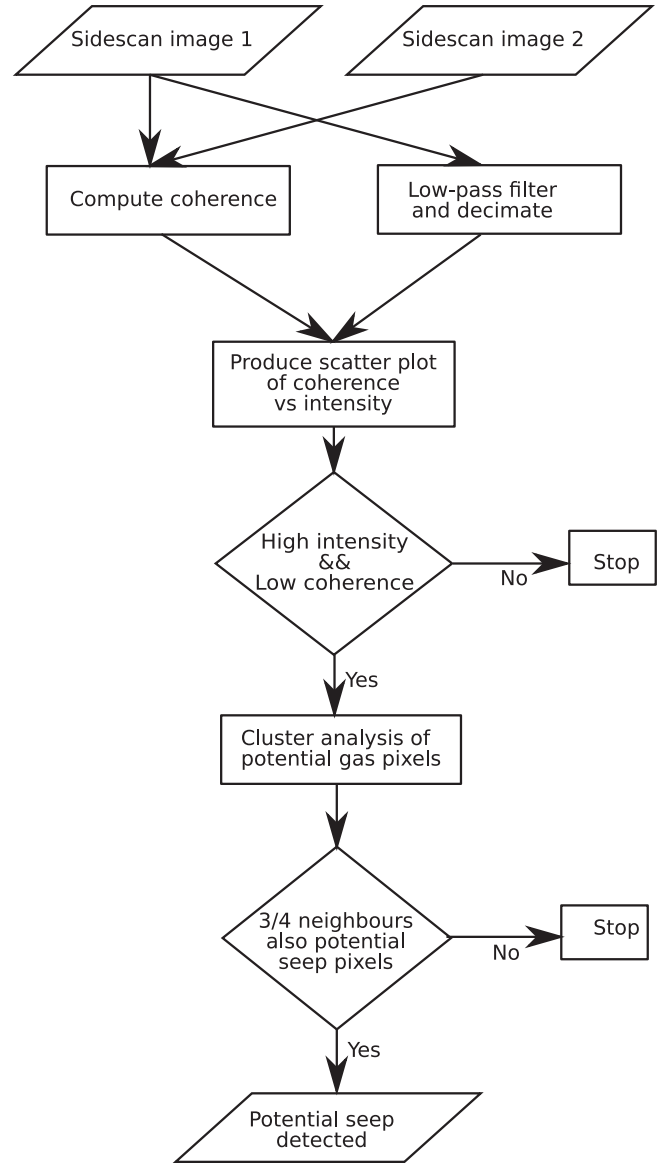


Fig. 3. Proposed method for gas seep detection.

illustrates the case when the seafloor reflections are mixed with reflections from two bubbles. Loss of vertical spatial coherence in the presence of bubbles has also been studied for the near-surface bubble layer [45].

III. METHOD FOR AUTOMATIC SEEP DETECTION USING AN INTERFEROMETRIC SIDESCAN SONAR

A new method for automatic gas seep detection based on an interferometric sidescan sonar is outlined by the flowchart in Fig. 3. The method takes as input the two complex-valued sidescan images produced from the two interferometric receiver arrays. The first step is to compute the interferometric coherence between the pair of images for each ping, using (6). We use a gliding correlation window of $N = 128$ pixels, equivalent to 3.2 m. Next, one of the sidescan images is lowpass filtered using a 2-m Hanning window in the cross-track direction, and decimated to match the cross-track resolution of the coherence



Fig. 4. The HISAS 1030 interferometric sonar mounted on the HUGIN AUV. This image was taken during recovery to the *G. O. Sars* research vessel.

map such that they have equal size and a scatter plot can be computed. We use the sidescan image from the upper receiver array. Alternatively, it is possible to use the sidescan image from the lower receiver array, or a combination of the two.

A scatter plot of the image intensity versus interferometric coherence illustrates the relationship between these two variables, and is the basis for the proposed detection algorithm. To facilitate on-the-fly seep detection and localization, we divide the image into processing patches. We let one patch consist of 100 pings (about 50 m), and the entire imaging cross-track range. We use a reference patch without gas seeps to compute statistics which are representative of the area. All pixels with a coherence value below a chosen threshold, and deviating significantly from a first-order polynomial best-fit curve to the scatter plot are considered potential gas pixels. We have found a reasonable coherence threshold to be 0.8, and defined “significant deviation” to be three standard deviations above the best-fit curve.

Finally, we analyze the geographical distribution of potential seep pixels. If they cluster into one or several confined regions, they are likely to originate from a seep location. We use the condition that a pixel is likely to originate from a seep if at least three out of the four nearest neighboring pixels are also potential seep pixels. For the final verification or dismissal of a potential seep, manual interpretation may be necessary.

IV. SIMULATIONS

We use the FOCUS toolbox [46] to design a set of simulations to test and demonstrate the proposed method. The simulations were designed to mimic the HISAS 1030 sonar (operating in sidescan mode) from which experimental results are presented in Section VI. The HISAS interferometric sonar mounted on the HUGIN AUV is shown in Fig. 4.

The simulated sonar system transmits a 4-ms linear FM chirp with a center frequency of 100 kHz and a bandwidth of 30 kHz, every 0.525 m. The horizontal and vertical 3-dB transmit beamwidths are approximately 15° and 45°, respectively. The interferometric receiver array consists of two sets of 32 ele-

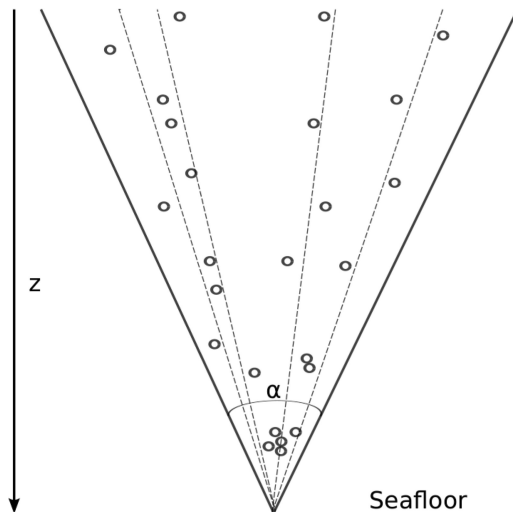


Fig. 5. Each simulated bubble follows a linear trajectory from the origin at the seafloor, to a random position within the cone defined by an opening angle α . The bubbles have small random movements in the horizontal plane relative to their trajectory, and rise at a constant speed of 0.2 m/s.

ments separated vertically by 30 cm. Each receiver element has a 23° horizontal and 46° vertical beamwidth. Before beamforming, we add white Gaussian noise to each channel, and apply a matched filter. Time-varying gain (TVG) is applied to compensate for range-dependent attenuation. We simulate a sonar altitude of 20-m above the seafloor.

A. Simulating a Stationary Scene

We constructed a stationary scene consisting of a flat seafloor and a container using 1 002 500 randomly distributed point scatterers (1 000 000 for the seafloor and 2500 for the container) with a Gaussian amplitude distribution. The container is 25 m wide, 5 m deep, and 5 m high. We simulate three different seafloor types with varying backscatter properties: silt, medium sand, and sandy gravel. We obtain seafloor scattering strengths from [47, Table III, Ch. IV]. Using a 100-kHz transmit frequency and the correct imaging geometry for our simulations (10° incidence angle from the horizontal at 100-m range), the approximate scattering strength is -35.7 dB for silt ($\alpha = 0.001$), -29.8 dB for medium sand, and -24.2 dB for sandy gravel. While the HISAS sonar is not absolutely calibrated, we obtain realistic levels of intensity of a given seafloor type relative to the expected intensity for the simulated bubble plume.

B. Simulating Gas Seeps

We simulate three gas seeps originating from each of the three seafloor types. The bubbles are simulated as point reflectors with intensities estimated using (3). We simulate bubble movement by allowing each bubble to follow a linear trajectory originating at the seafloor and spreading conically by an angle α . Fig. 5 shows an example of a 2-D time snapshot of simulated bubble positions. Each bubble trajectory ends at a given height above the seafloor (maximum rise height for the given seep) and at a random xy -position within the cone. Each bubble has

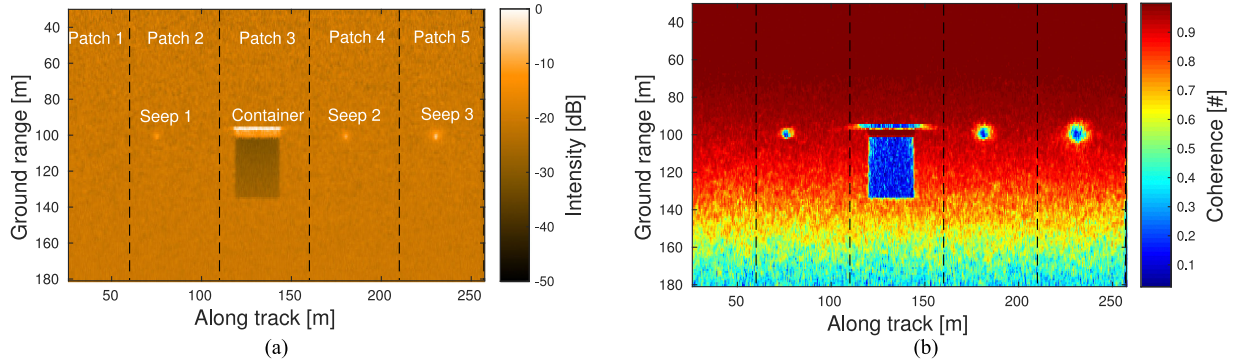


Fig. 6. Simulated scene containing a container and three gas seeps on a sandy seafloor. The sidescan image intensity (a) is high at the front wall of the container as well as at the three seep locations. The interferometric coherence (b) is generally high, except at the seep locations, in the acoustic shadow region behind the container, and in the region in front of the container affected by layover effects.

small random horizontal movements (between -2 and 2 mm) relative to its trajectory, and rises at a constant vertical speed of 0.2 m/s. In lack of knowledge about the expected bubble size distributions, we simulate bubbles with a constant 5 -mm radius. Multiple scattering from within the bubble plume is not included in this model. Acoustic shadow effects are included for the solid container, but not for the bubble plume.

We simulate three seeps. Seep 1 consists of 15 bubbles per vertical meter and a plume height of 10 m above the seafloor. Seep 2 consists of 60 bubbles per vertical meter, and rises to a height of 20 m. Seep 3 consists of 145 bubbles per vertical meter and rises to 40 m above the seafloor. All three seeps have a spreading angle $\alpha = 30^\circ$.

V. RESULTS FROM SIMULATIONS

Fig. 6(a) shows a sidescan image of the simulated scene, and Fig. 6(b) shows the interferometric coherence map of the same scene, produced using (6). The seafloor in this case consists of medium sand. The three seeps are visible in the sidescan image as regions of high intensity relative to the background, and as regions of low interferometric coherence in the coherence map. The scene is divided into five 50 -m along-track processing patches, and each patch is analyzed using the method described in Section III.

We observe that the coherence is low at the seep locations due to the presence of many vertically distributed scatterers within the correlation window, as expected. The coherence is also low in the shadow region behind the container where random noise dominates due to the lack of signal, and at far range where the signal intensity drops due to range-dependent attenuation while the average noise level remains constant. Finally, the coherence is low in front of the container, where layover effects cause the reflections from the seafloor to become mixed with those from the front edge of the container.

Fig. 7 shows scatter plots of intensity versus interferometric coherence for patches 1, 2, 3, 4, and 5.

Patch 1: Patch 1 consists of a sandy seafloor without the presence of seeps or other objects. The scatter plot from this area [Fig. 7(a)] shows a pixel distribution which is centered

around a mean intensity of about -20 dB (indicated by the pink line), and interferometric coherence values ranging from 0.2 to 1 . The red and blue lines indicate two and three standard deviations, respectively. For a Rayleigh process such as fully developed speckle, the expected value of the mean value divided by the standard deviation is 1.91 [48]. In a practical setting, this may not hold. We use patch 1 as a reference patch from which we estimate the polynomial best-fit curve, its mean, and standard deviations. When computing the reference statistics we disregard strong, coherent scatterers found in the yellow shaded upper righthand corners of the scatter plots in Fig. 7. These pixels do not represent potential gas pixels, and skew the otherwise symmetric seafloor response. There are no potential gas pixels in patch 1.

For illustration purposes, we have color shaded four regions in the scatter plots representing different scenarios. Based on our discussion in Section II-D, we expect gas pixels to have a high image intensity as well as low interferometric coherence. This corresponds to the red shaded area in the upper lefthand part of the scatter plots in Fig. 7. Note that pixels affected by layover share these characteristics and will appear in the same region in the scatter plot. Other high-intensity noise sources such as acoustical interference may also appear in this region and are considered potential sources of false alarms. The gray region represents pixels with low image intensity and low interferometric coherence. In this area, we expect to find pixels from within acoustical shadow regions, or far range pixels with sufficiently low image intensity. In the violet area, we only expect to find highly coherent pixels representing the seafloor itself but with low image intensity. As the intensity decreases, noise will begin to dominate and the coherence drop, pulling pixels toward the gray region. The yellow region represents pixels from strong, coherent scatterers such as rocks and other objects on the seafloor.

Patch 2: Patch 2 [Fig. 7(b)] contains a small gas seep with 15 bubbles per vertical meter of water. The solid red circles represent detected seep pixels (high intensity and low coherence, as well as clustering into a confined region). The cyan pixels represent pixels that were detected as potential gas pixels because they appear in the red shaded area in the scatter plot, but

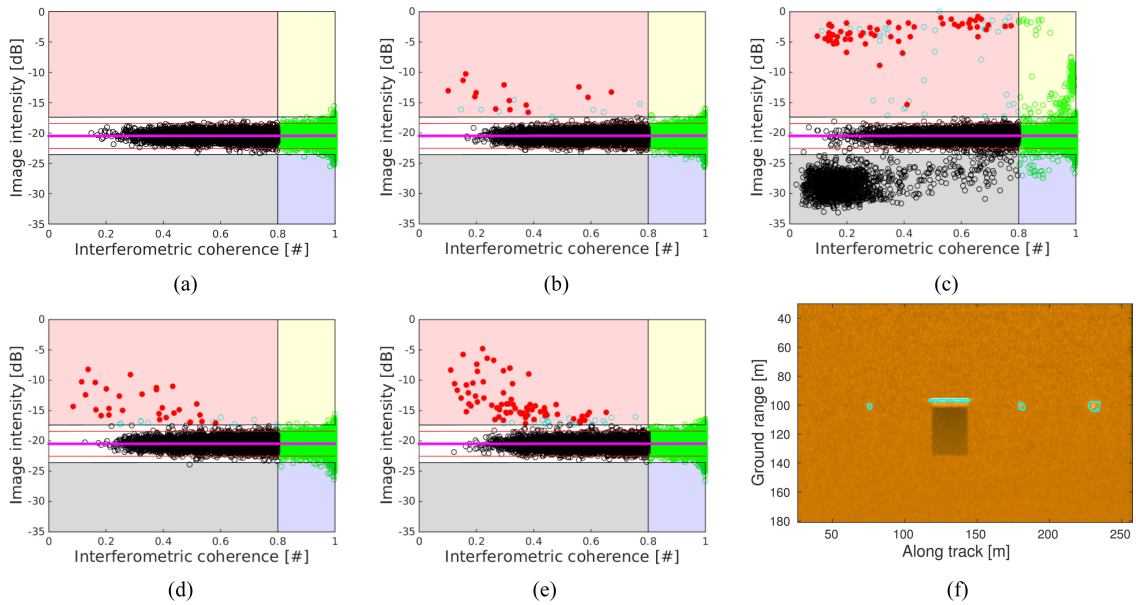


Fig. 7. Scatter plots and potential seep pixels from: (a) patch 1 (no seep), (b) patch 2 (small seep), (c) patch 3 (container), (d) patch 4 (medium seep), and (e) patch 5 (large seep) in the simulated scene. Red circles represent detected seep pixels, and cyan circles represent potential seep pixels that are discarded in the cluster analysis phase. Black and green pixels represent seafloor scattering and are not considered potential seep pixels. (f) Sidescan image of the scene with detected seep pixels indicated.

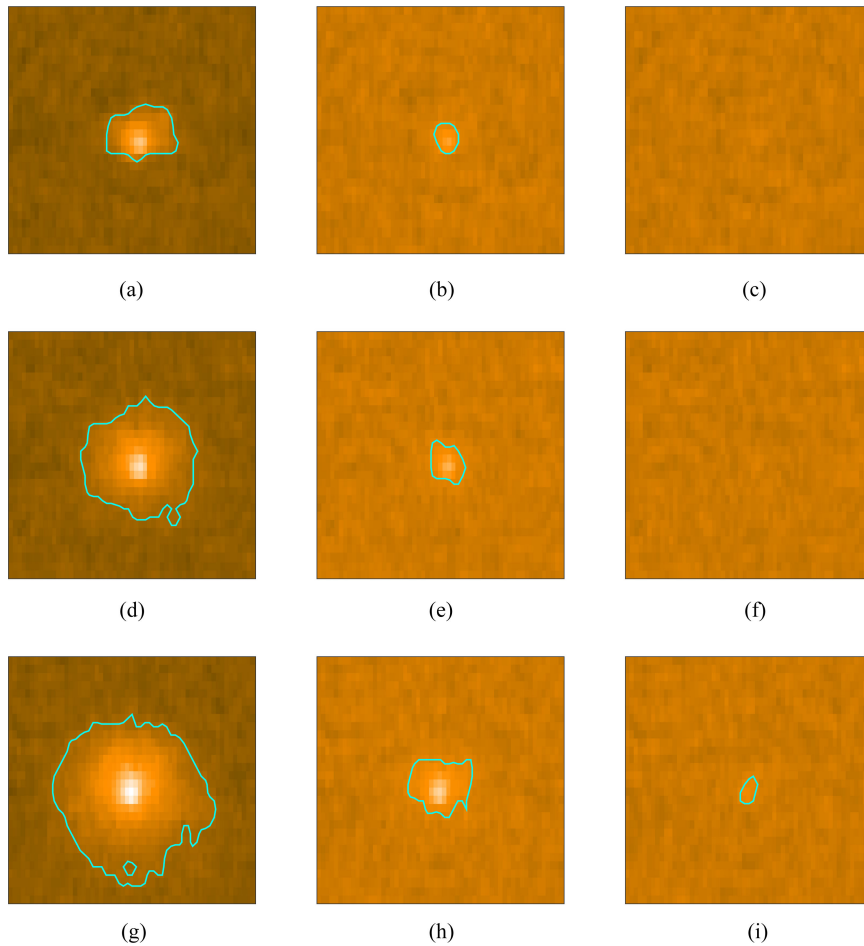


Fig. 8. Seep detectability for varying simulated seafloor types. (a)–(c) Sidescan intensity images of seep 1 for silt, sand, and gravel, respectively. (d)–(f) Intensity images of seep 2 for silt, sand and gravel. (g)–(i) Images of seep 3 for the same seafloor types. Each image shows a 30-m \times 30-m patch of the seafloor, displayed with a 50-dB dynamic range.

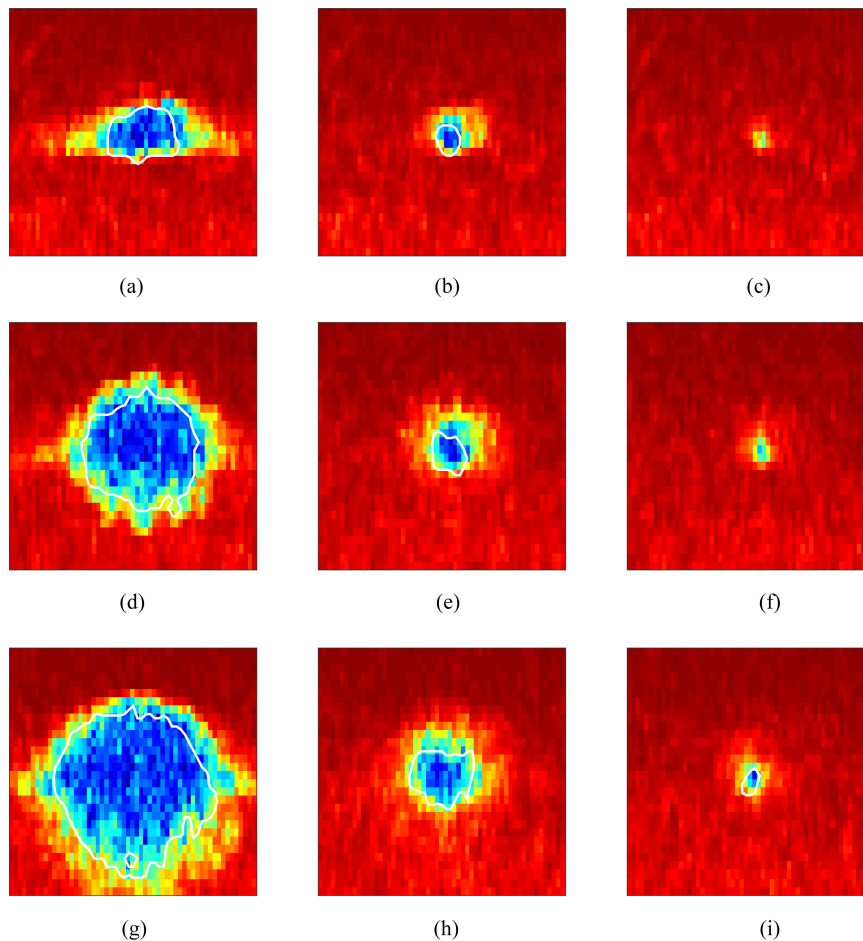


Fig. 9. Interferometric coherence maps from the same regions and simulated seafloor types as in Fig. 8. (a)–(c) Coherence maps for seep 1 for silt, sand, and gravel. (d)–(f) Coherence maps for seep 2. (g)–(i) Coherence maps for seep 3. The colormap ranges from 0 (blue) to 1 (red).

discarded since they do not cluster into a confined region. These pixels originate from the boundary of the seep location, with less than three detected neighboring seep pixels. The circumference of the automatically detected seep is indicated in Fig. 7(f).

Patch 3: False alarms may occur in regions where the image intensity is high and the interferometric coherence is low. This may be the case when there is considerable noise such as acoustic interference from other equipment, or in the presence of elevated objects giving rise to geometrical distortion (layover). The front wall of the container in patch 3 is an example of an elevated object causing layover effects in the image. The front wall is visible in the sidescan image as a bright region at a closer range than its true position. The interferometric coherence in this region is low, since the received echo is a mix of the seafloor return and the return from the upper edge of the front wall. Pixels falsely detected as gas seeps are shown as red circles in Fig. 7(c) and indicated along the front wall of the container in Fig. 7(f). Again, the cyan circles represent potential seep pixels along the boundary of the layover region, which are discarded during the clustering analysis.

Patch 3 also contains considerable pixels in the lower left part of the scatter plot [gray area in Fig. 7(c)], originating from the shadow region behind the container. The container itself is a strongly and coherently scattering object, resulting in the green

pixels in the upper right hand corner [yellow area in Fig. 7(c)]. There are also a few green pixels at the top of the same area, originating from the layover region in front of the container. Since we use a window to compute the coherence, the transition from high to low coherence is gradual, resulting in a few pixels with coherence ≥ 0.8 and high image intensity.

Patches 4 and 5: The seeps in patches 4 and 5 [Fig. 7(d) and (e)] are easily detected on this seafloor type.

A. The Effects of Seafloor Characteristics

The ability to detect a seep depends on the flux and bubble size distribution of the seep, the distance from the sonar (the sonar footprint increases as a function of range), the sonar system (transmit frequency, beamwidth, and SNR), and the seafloor type. Keeping everything else constant, we evaluate the detectability of a given seep for three different seafloor types: silt, medium sand, and sandy gravel. The same seep is more easily detected on a seafloor with low backscatter strength such as silt, than on a highly scattering seafloor such as gravel or rock. Fig. 8 shows a 30-m \times 30-m region of the intensity image for each seafloor type. The structure of the seafloor is not realistic (gravel stone structures are not visible), but the image intensity is at a realistic level. Detected seep pixels, if any, are indicated by the blue line.

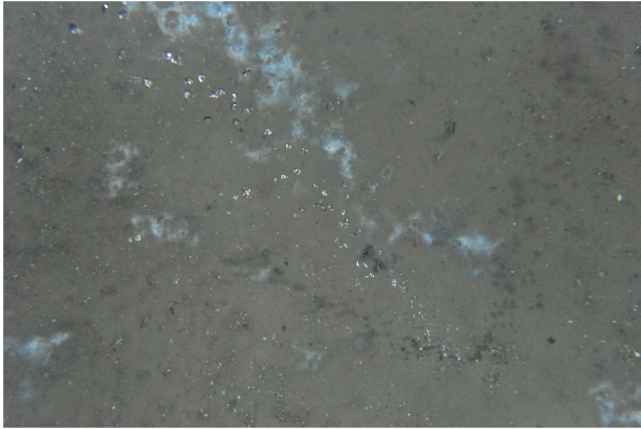


Fig. 10. Image of methane bubbles ascending from well 15/9-11. The image was taken with a Nikon D3 still camera mounted on an ARGUS ROV. The image was taken approximately two meters above the seafloor.

Fig. 9 shows the coherence maps for the same regions. Note that seeps 1 and 2 are not visible in the sidescan image for the simulated gravel seafloor [Fig. 8(c) and (f)], but appear as regions of low coherence [Fig. 9(c) and (f)]. This indicates that these seeps are detectable despite not being visible in the intensity image. This is similar to techniques described in coherent change detection in radar [49], also discussed in sonar [50]. We have chosen a conservative set of parameters to minimize the number of false alarms, and for these parameters these small seeps are not detected on a gravel seafloor.

VI. REAL DATA RESULTS FROM TWO LEAKING WELLS IN THE NORTH SEA

We verify our results using field data collected using the HISAS 1030 interferometric SAS [14] mounted on a HUGIN AUV during sea trials in the North Sea in 2011 and 2012. During acquisition, HUGIN operated at 20-m height above the seafloor, covering more than 1 km² per hour in relatively flat terrain. The HISAS sonar operates at a center frequency of 100 kHz and has a 30-kHz bandwidth. In this work, we do not take advantage of the synthetic aperture sonar capabilities of the HISAS sonar, but apply the seep detection algorithm to conventional sidescan data.

Several gas seeps are located in the area, originating from abandoned wells leaking small amounts of shallow methane gas. The water depth in this area is about 80 m, and the seafloor is flat and consists mainly of sand with scattered shell-rich patches (shell hash). We present results from two abandoned leaking wells, well 16/4-2 and well 15/9-11. The photograph shown in Fig. 10 is from well 15/9-11, and was taken during a remotely operated vehicle (ROV) dive.

Fig. 11(a) shows the sidescan image for well 16/4-2, and Fig. 11(b) shows the corresponding coherence map. The scatter plots from four example patches are shown in Fig. 12. High intensity and high coherence indicates strongly scattering, coherent scatterers. Patch 1 contains a few strongly scattering rocks giving rise to the “tail” of green pixels in the upper right corner of the scatter plot in Fig. 12(a). We use patch 1 as a ref-

erence patch, again disregarding strong, coherent pixels since they do not represent potential seep pixels, and their presence skews the otherwise symmetric response from the seafloor. A single pixel at far range (≈ 180 m) in Patch 1 is falsely detected as a seep-related pixel. It is shown as a red pixel in the scatter plot in Fig. 12(a). When analyzing the entire image, three more far-range pixels are falsely detected at approximate along-track ranges 320, 340, and 555 m. Manual inspection of the sidescan image and coherence map indicates that all four falsely detected pixels are related to self-generated noise.

The seep located in patch 2 is correctly detected. Red circles in Fig. 12 represent detected seep pixels, and cyan pixels represent potential seep pixels that were discarded as noise since they do not cluster into one or several confined regions. The circumference of the detected seep pixels in Fig. 12(b) is indicated in Fig. 11(a).

Fig. 13 show the sidescan image and interferometric coherence map from well 15/9-11. Patch 1 is used as a reference patch, and the seep in patch 2 with a characteristic “flare” shape is correctly detected. In this case, the flare shape is caused by horizontal bubble movements due to currents. In contrast, multi-beam and single-beam images of gas plumes often have a similar shape due to the upward movement of bubbles. There were no false alarms at this site.

VII. DISCUSSION

The method proposed here is developed for robust, automatic detection and detailed localization of marine gas seeps. The seafloor characteristics have a significant impact on the method’s ability to detect small seeps. To be detectable, a seep has to have a total backscattered cross section which is greater than or comparable to that of the seafloor. When this is the case, the interferometric coherence is low.

Depending on the chosen parameters, it is possible to detect a seep even if it is not visible in the sidescan intensity image. This is the case for seeps 2 and 3 in the simulated gravel seafloor in Fig. 8. If we reduce the threshold for potential seep pixels from three to two standard deviations from the best-fit curve, all three seeps are detected for all seafloor types, and no additional false alarms are introduced. In contrast, if we use the stricter clustering condition that all four nearest neighboring pixels must also be potential seep pixels, the false alarms caused by the layover region in front of the container in Fig. 7, as well as the four far-range false alarms in Fig. 11, are removed. We choose a conservative set of parameters to minimize the probability of not detecting a seep, while maintaining an acceptable false alarm rate.

We use a reference patch which is representative of the seafloor in the general area, and apply a simple linear polynomial best fit model to the scatter plot to compute the necessary statistics. A more sophisticated statistical approach might be beneficial, but results from simulations and field data indicate that a linear model is sufficient. In areas of rapidly changing seafloor characteristics, the reference patch may be updated either at regular intervals or continuously to ensure that it is representative of the current seafloor type. We have found that

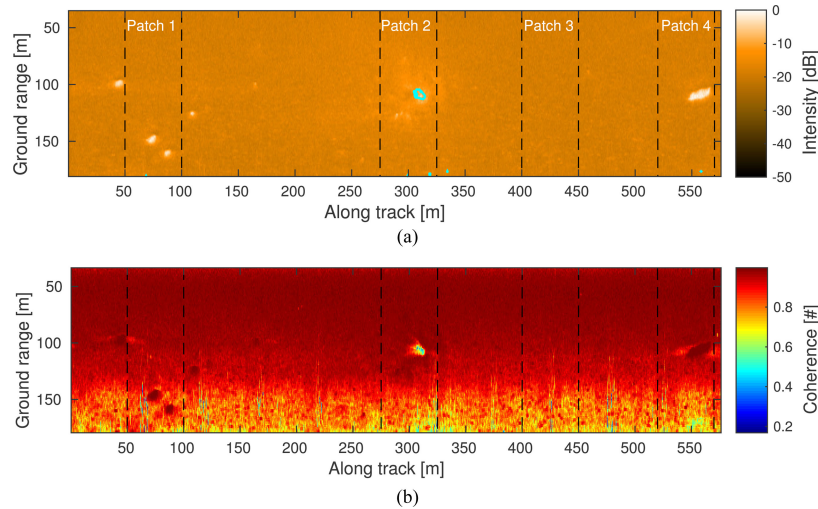


Fig. 11. (a) Sidescan sonar image and (b) interferometric coherence map of a portion of the seafloor in the North Sea, acquired using the HISAS 1030 sonar mounted on the HUGIN AUV. A small methane seep originating from abandoned well 16/4-2 is detected and indicated by the blue circle in (a).

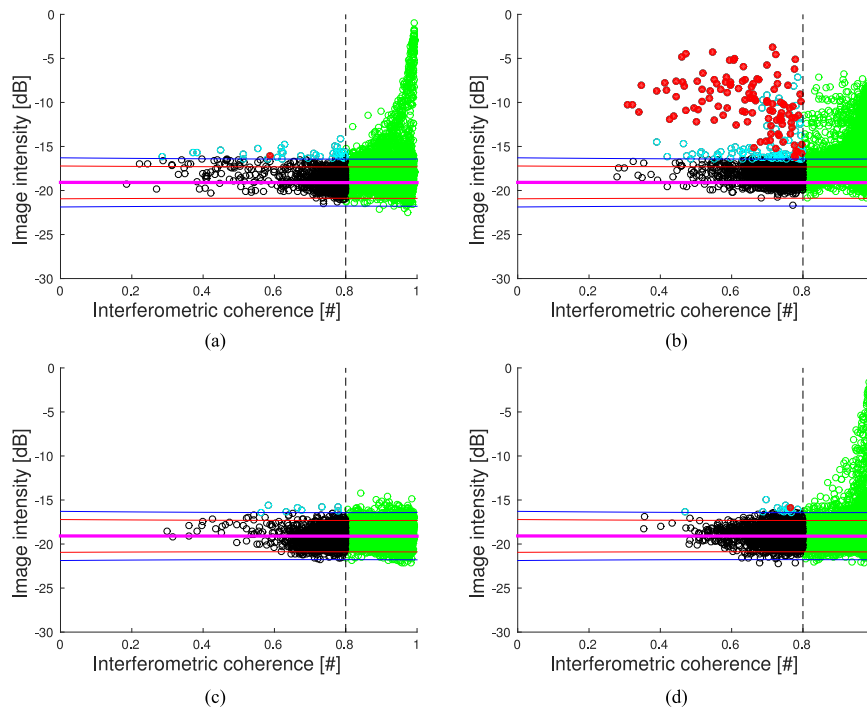


Fig. 12. Scatter plots for patches 1, 2, 3, and 4 from the field data shown in Fig. 11. Red circles represent detected seep pixels, and cyan pixels represent potential seep pixels that were discarded as noise since they do not cluster into one or several confined regions.

the choice of reference patch is not critical, and that the method works satisfactory even without the use of a reference patch, as long as the processing patch from which the statistics are computed is large compared to the seep. If the statistics are computed directly from the current processing patch, small seeps may be missed. The reason for this is that the intensity spread increases in the presence of a seep, resulting in a higher seep threshold (the blue three standard deviation lines move upward), unless the seep is small relative to the processing patch.

The HISAS sonar is, like most sidescan sonars today, not absolutely calibrated. As a result, there is not a predictable relationship between the measured echo intensity and the target

strength of the insonified volume. It is possible, however, to reveal changes in the intensity and spatial extent of a seep over time, as well as make relative comparisons of different seeps. It is not possible to determine the plume height or quantify the amount of leakage using this method. Since the sonar travels near the seafloor, only the first 20–30 m of the plume is included in the analysis. In a comprehensive monitoring solution, the proposed automatic detection method should be complemented by additional sensors for seep characterization and quantification.

False alarms occur in regions where the sonar image is affected by geometric distortion, but these are often predictable and can be rejected by visual inspection. Fish represent a

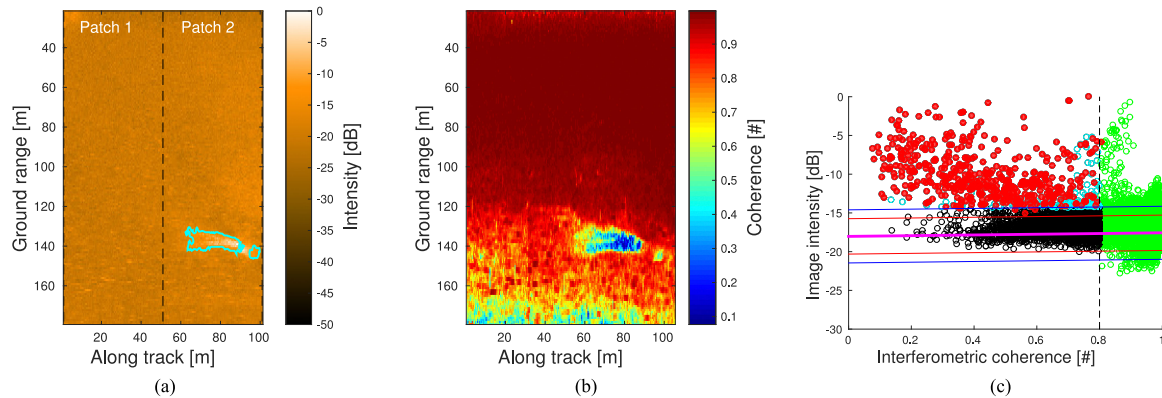


Fig. 13. (a) Sidescan sonar image and (b) interferometric coherence map of a portion of the seafloor including the abandoned North Sea well 15/9-11. The scatter plot with detected seep pixels is shown in (c). The images were acquired using the HUGIN-mounted HISAS 1030 sonar.

challenge, since they are acoustically very similar targets to bubbles. This is the topic of a Ph.D. dissertation [51], where the conclusion is that it is possible to differentiate between fish and bubbles by analyzing the frequency response combined with the spatial distribution and temporal variations in the measured acoustic response. However, this requires a longer observation period than what is achievable with a single pass with an AUV.

Finally, it is worth noting that this method can be applied to any interferometric sidescan system. We use an interferometric SAS system, operated in sidescan mode. This has additional advantages, since potential seep locations are detected and combined with simultaneously acquired and colocated high-resolution seafloor imagery and bathymetry. Using this approach gas seeps are automatically detected, while visual inspection of the SAS imagery can reveal the presence of other indications of leakage including pock marks and bacterial mats. The area coverage rate of an AUV-mounted sonar depends on the topography, background noise levels, and the sonar's speed and height above the seafloor. Typical values for a HUGIN AUV equipped with the HISAS sonar are 1–2 km²/h. In low-SNR conditions or extreme topography, the effective coverage rate may be lower due to limitations in the seep detection range.

VIII. CONCLUSION

Marine gas seeps may occur in a range of scenarios including naturally occurring methane or CO₂ seepage, as well as leaks related to oil and gas production or subseafloor CO₂ storage. Detecting marine gas seeps is essential to obtain realistic estimates of the amount of greenhouse gases entering the oceans and potentially reaching the atmosphere, and to minimize potential environmental and economical consequences of offshore leakage.

Existing methods for marine gas seep detection leave room for improvement, especially when it comes to the ability to cover large areas and to automatically detect and localize seeps. We propose a method for automatic detection of marine gas seeps using an AUV-mounted interferometric sidescan sonar. Through simulations, we demonstrate that it is possible to detect small gas seeps using the HISAS 1030 sonar. We investigate seep detectability for three different seafloor types ranging from silt

to sandy gravel. We verify our results using field data from two North Sea wells leaking small amounts of methane gas.

ACKNOWLEDGMENT

The authors would like to thank the crew of the research vessel *G. O. Sars*, and the HUGIN AUV operators. They would also like to thank Dr. F. Prieur and Prof. A. Lyons for valuable input regarding bubble acoustics.

REFERENCES

- [1] A. G. Judd, "The global importance and context of methane escape from the seabed," *Geo-Marine Lett.*, vol. 23, no. 3–4, pp. 147–154, 2003.
- [2] J. Blackford *et al.*, "Detection and impacts of leakage from sub-seafloor deep geological carbon dioxide storage," *Nature Clim. Change*, vol. 4, no. 11, pp. 1011–1016, 2014.
- [3] A. Nikolovska, H. Sahling, and G. Bohrmann, "Hydroacoustic methodology for detection, localization, and quantification of gas bubbles rising from the seafloor at gas seeps from the eastern black sea," *Geochem. Geophys. Geosyst.*, vol. 9, no. 10, 2008, DOI: 10.1029/2008GC002118.
- [4] X. Lurton, *An Introduction to Underwater Acoustics: Principles and Applications*, Chichester, U.K.: Springer-Praxis, 2002.
- [5] J. Schneider von Deimling, J. Brockhoff, and J. Greinert, "Flare imaging with multibeam systems: Data processing for bubble detection at seeps," *Geochem. Geophys. Geosyst.*, vol. 8, no. 6, 2007.
- [6] S. Dupré *et al.*, "High-resolution mapping of large gas emitting mud volcanoes on the Egyptian continental margin (Nile Deep Sea Fan) by AUV surveys," *Mar. Geophys. Res.*, vol. 29, no. 4, pp. 275–290, 2008.
- [7] T. C. Weber *et al.*, "Mapping gas seeps with the deepwater multibeam echosounder on Okeanos Explorer," *Oceanography*, vol. 25, no. 1, 2012.
- [8] S. Dupré, J. Woodside, I. Klaucke, J. Masclé, and J.-P. Foucher, "Widespread active seepage activity on the Nile Deep Sea Fan (offshore Egypt) revealed by high-definition geophysical imagery," *Mar. Geol.*, vol. 275, no. 14, pp. 1–19, 2010.
- [9] T. G. Leighton and P. R. White, "Quantification of undersea gas leaks from carbon capture and storage facilities, from pipelines and from methane seeps, by their acoustic emissions," *Proc. Roy. Soc. A, Math. Phys. Eng. Sci.*, vol. 468, no. 2138, pp. 485–510, Oct. 2011.
- [10] B. J. Bergès, T. G. Leighton, and P. R. White, "Passive acoustic quantification of gas fluxes during controlled gas release experiments," *Int. J. Greenhouse Gas Control*, vol. 38, pp. 64–79, 2015.
- [11] T. C. Weber, K. Jerram, and L. Mayer, "Acoustic sensing of gas seeps in the deep ocean with split-beam echosounders," in *Proc. Eur. Conf. Underwater Acoust.*, Istanbul, Turkey, Jul. 2010, pp. 189–195.
- [12] T. C. Weber *et al.*, "Estimating oil concentration and flow rate with calibrated vessel-mounted acoustic echo sounders," *Proc. Nat. Acad. Sci.*, vol. 109, no. 50, pp. 20 240–20 245, Dec. 2011.
- [13] A. E. A. Blomberg, C.-I. C. Nilsen, T. O. Sæbø, R. E. Hansen, and A. Austeng, "Detecting and localizing gas seeps at the seafloor using an interferometric sidescan sonar," in *Proc. 11th Eur. Conf. Underwater Acoust.*, vol. 34, 2012, pp. 597–604.

- [14] T. G. Fossum, P. E. Hagen, B. Langli, and R. E. Hansen, "HISAS 1030: High resolution synthetic aperture sonar with bathymetric capabilities," *Shallow Survey*, Oct. 2008.
- [15] I. Leifer, M. J. Kamerling, B. P. Luyendyk, and D. S. Wilson, "Geologic control of natural marine hydrocarbon seep emissions, Coal Oil Point seep field, California," *Geo-Marine Lett.*, vol. 30, no. 3-4, pp. 331-338, Mar. 2010.
- [16] K. Anthony, P. Anthony, G. Grosse, and J. Chanton, "Geologic methane seeps along boundaries of arctic permafrost thaw and melting glaciers," *Nature Geosci.*, vol. 5, no. 6, pp. 419-426, 2012.
- [17] A. Judd, M. Hovland, L. Dimitrov, S. Garcia Gil, and V. Jukes, "The geological methane budget at continental margins and its influence on climate change," *Geofluids*, vol. 2, no. 2, pp. 109-126, 2002.
- [18] S. A. Zimov, E. A. Schuur, and F. S. Chapin III, "Permafrost and the global carbon budget," *Science*, vol. 312, no. 5780, pp. 1612-1613, 2006.
- [19] Official Journal of the European Union, "Directive 2009/31/EC of the European Parliament and of the Council of 23 April 2009 on the geological storage of carbon dioxide and amending Council Directive 85/337/EEC, European Parliament and Council Directives 2000/60/EC, 2001/80/EC, 2004/35/EC, 2006/12/EC, 2008/1/EC and Regulation (EC) No 1013/2006," 1140/114.
- [20] A. Chadwick, R. Arts, O. Eiken, P. Williamson, and G. Williams, "Geophysical monitoring of the CO₂ plume at Sleipner, North Sea," *Adv. Geological Storage of Carbon Dioxide*, Berlin, Germany: Springer-Verlag, 2006, pp. 303-314.
- [21] "SUCCESS annual report 2015," 2015. [Online]. Available: <http://www.fme-success.no/index.cfm?id=364686>
- [22] ECO2, "Best practice guidance for environmental risk assessment for offshore CO₂ geological storage," ECO2, Tech. Rep., 2015.
- [23] J. Blackford, H. Stahl, J. Kita, and T. Sato, "Preface to the QICS special issue," *Int. J. Greenhouse Gas Control*, no. 38, p. 1, 2015.
- [24] J. Blackford *et al.*, "Marine baseline and monitoring strategies for carbon dioxide capture and storage (CCS)," *Int. J. Greenhouse Gas Control*, vol. 38, pp. 221-229, 2015. [Online]. Available: <http://oceanrep.geomar.de/29147/>
- [25] W. E. Sweet, "Marine acoustical seep detection," *AAPG Bull.*, vol. 58, no. 6, pp. 1133-1136, 1974.
- [26] G. Meinecke, M. Roemer, H. Sahling, and G. Bohrmann, "Hydroacoustic mapping of gas bubble emissions at the don-kuban paleo-fan (Black Sea) using ship-mounted and AUV-based sonar systems," in *Proc. 11th Eur. Conf. Underwater Acoust.*, 2013, pp. 910-917.
- [27] I. Leifer and D. Tang, "The acoustic signature of marine seep bubbles," *J. Acoust. Soc. Amer.*, vol. 121, no. 1, p. EL35, 2007.
- [28] G. Wendelboe, S. Barchard, E. Maillard, and L. Bjorno, "High-resolution multibeam sonar for subsea leakage detection," in *Proc. Meetings Acoust.*, vol. 17, no. 1, 2014, 070094.
- [29] J. S. von Deimling and C. Papenberg, "Technical note: Detection of gas bubble leakage via correlation of water column multibeam images," *Ocean Sci.*, vol. 8, no. 2, pp. 175-181, Mar. 2012.
- [30] S. M. Wiggins, I. Leifer, P. Linke, and J. A. Hildebrand, "Long-term acoustic monitoring at north sea well site 22/4b," *Mar. Petroleum Geol.*, vol. 68, pp. 776-788, 2015.
- [31] T. G. Leighton, *The Acoustic Bubble*, London, U.K.: Academic 1997, ch. 3.
- [32] H. Medwin and C. S. Clay, *Fundamentals of Acoustic Oceanology*. Boston, MA, USA: Academic 1998, Ch. 8.
- [33] V. C. Anderson, "Sound scattering from a fluid sphere," *J. Acoust. Soc. Amer.*, vol. 22, no. 4, pp. 426-431, 1950.
- [34] I. Leifer and D. Culling, "Formation of seep bubble plumes in the Coal Oil Point seep field," *Geo-Marine Lett.*, vol. 30, no. 3-4, pp. 339-353, 2010.
- [35] M. S. Salmi, H. P. Johnson, I. Leifer, and J. E. Keister, "Behavior of methane seep bubbles over a pockmark on the cascadia continental margin," *Geosphere*, vol. 7, no. 6, pp. 1273-1283, 2011.
- [36] T. C. Weber, L. A. Mayer, J. Beaudoin, Y. Rzhano, and D. Lovalvo, "Acoustic estimates of methane gas flux from the seabed in a 6000 km² region in the northern gulf of mexico," *Geochem. Geophys. Geosyst.*, vol. 15, no. 5, pp. 1911-1925, 2014.
- [37] M. Strasberg, "The pulsation frequency of nonspherical gas bubbles in liquids," *J. Acoust. Soc. Amer.*, vol. 25, no. 3, pp. 536-537, 1953.
- [38] D. E. Weston, "Sound propagation in the presence of bladder fish," *Underwater Acoust.*, vol. 2, pp. 55-88, 1967.
- [39] M. A. Ainslie and T. G. Leighton, "Near resonant bubble acoustic cross-section corrections, including examples from oceanography, volcanology, and biomedical ultrasound," *J. Acoust. Soc. Amer.*, vol. 126, no. 5, pp. 2163-2175, 2009.
- [40] M. A. Ainslie and T. G. Leighton, "Review of scattering and extinction cross-sections, damping factors, and resonance frequencies of a spherical gas bubble," *J. Acoust. Soc. Amer.*, vol. 130, no. 5, pp. 3184-3208, 2011.
- [41] T. O. Sæbø, "Seafloor depth estimation by means of interferometric synthetic aperture sonar," Ph.D. dissertation, Universitetet i Tromsø, Tromsø, Norway, 2010.
- [42] R. F. Hanssen, *Radar Interferometry: Data Interpretation and Error Analysis*, Dordrecht, The Netherlands: Kluwer, 2001, Ch. 4.3.
- [43] H. Zebker and J. Villaseñor, "Decorrelation in interferometric radar echoes," *IEEE Trans. Geosci. Remote Sens.*, vol. 30, no. 5, pp. 950-959, 1992.
- [44] S. A. Synnes, R. E. Hansen, and T. O. Sæbø, "Assessment of shallow water performance using interferometric sonar coherence," in *Proc. Underwater Acoust. Measur.*, Nafplion, Greece, Jun. 2009.
- [45] S. T. McDaniel, "Vertical spatial coherence of backscatter from bubbles," *IEEE J. Ocean. Eng.*, vol. 12, no. 2, pp. 349-356, 1987.
- [46] R. E. Hansen, T. O. Sæbø, H. J. Callow, P. E. Hagen, and E. Hammerstad, "Synthetic aperture sonar processing for the HUGIN AUV," in *Proc. OCEANS Eur.*, vol. 2, Brest, France, 2005, pp. 1090-1094.
- [47] *APL-UW High-Frequency Ocean Environmental Acoustic Models Handbook*, Appl. Phys. Lab., Univ. Washington, Seattle, WA, USA, Oct. 1994.
- [48] R. F. Wagner, S. W. Smith, J. M. Sandrik, and H. Lopez, "Statistics of speckle in ultrasound B-scans," *IEEE Trans. Sonics Ultrasonics*, vol. 30, no. 3, pp. 156-163, 1983.
- [49] M. Preiss and N. J. S. Stacy, "Coherent change detection: Theoretical description and experimental results," Defence Science and Technology (DSTO), Australia, Tech. Rep. DSTO-TR-1851, Aug. 2006.
- [50] V. L. Myers, D. D. Sternlicht, A. P. Lyons, and R. E. Hansen, "Automated seabed change detection using synthetic aperture sonar: Current and future directions," in *Proc. Synthetic Aperture Sonar Synthetic Aperture Radar*, Lercic, Italy, Sep. 2014.
- [51] R. Kubilius, "Multi-frequency acoustic discrimination between gas bubble plumes and biological targets in the ocean," Ph.D. dissertation, Univ. Bergen, Norway, 2015.



Ann Elisabeth Albright Blomberg was born in Falun, Sweden, in 1979. She received the M.Sc. degree in signal processing and the Ph.D. degree from the Department of Informatics, University of Oslo, Oslo, Norway, in 2005 and 2012, respectively.

From 2005 to 2008, she worked as a Processing Geophysicist at CGGVeritas, Høvik, Norway. She is currently working as a postdoctoral research fellow at the Digital Signal Processing and Image Analysis group at the University of Oslo, and also holds a part-time position at the Norwegian Geotechnical

Institute (NGI). Her research interests include sonar and medical ultrasound imaging, adaptive beamforming, and the application of geophysical methods for marine gas seep detection and monitoring.



Torstein Olsmo Sæbø (M'06-SM'13) was born in Bergen, Norway, in 1977. He received the cand.scient (M.Sc.) degree in astrophysics from the University of Oslo, Oslo, Norway, in 2002 and the Ph.D. degree in physics from the University of Tromsø, Tromsø, Norway, in 2010, with a dissertation entitled Seafloor depth estimation by means of interferometric synthetic aperture sonar.

Since 2002, he has been with the Norwegian Defence Research Establishment (FFI), Kjeller, Norway, specializing in the field of interferometry on synthetic aperture sonar. He is currently Research Manager for the marine robotics development and the synthetic aperture sonar development at FFI, Kjeller, Norway, specializing in the field of interferometry on synthetic aperture sonar.

Dr. Sæbø is an Associate Editor of the IEEE JOURNAL OF OCEANIC ENGINEERING.



Roy Edgar Hansen (M'07-SM'16) received the M.Sc. degree in physics in 1992, and the Ph.D. degree in physics in 1999, both from the University of Tromsø, Norway. His Ph.D. thesis was entitled Measurements in the Mixed Layer by a Bistatic Multi-CW Doppler Sonar.

From 1992 to 2000 he was with the Norwegian research company TRIAD, working on multistatic sonar, multistatic radar, SAR and underwater communications. Since 2000, he has been working at the Norwegian Defence Research Establishment (FFI), Kjeller, Norway, in the field of synthetic aperture sonar. He is currently principal scientist at FFI. He is also an Adjunct Associated Professor at the Department of Informatics, University of Oslo, Oslo, Norway.



Andreas Austeng (M'97) was born in Oslo, Norway, in 1970. He received the M.S. degree in physics and the Ph.D. degree in computer science from the University of Oslo, Oslo, Norway, in 1996 and 2001, respectively.

Since 2001 he has been working at the Department on Informatics, University of Oslo, first as a Postdoctoral Research Fellow, and currently as an Associate Professor. His research interests include signal processing for acoustical imaging.



Rolf Birger Pedersen received the Dr. Philos. degree in geology from the University of Bergen, Bergen, Norway, in 1992.

He is now Professor at the University of Bergen. A central theme of his research has been on the deep sea and the formation of oceanic lithosphere. He has been leading a number of international sea-going expeditions where seafloor mapping, imaging and sampling have been essential. He is currently the Director of the Centre for Geobiology, which is a Norwegian Centre of Excellence focusing on deep-sea research and geobiological interactions.